Modeling and simulation of strain-induced phase transformations under compression in a diamond anvil cell

Valery I. Levitas[1,2,3,*] and Oleg M. Zarechnyy[2]
[1]*Department of Mechanical Engineering, Iowa State University, Ames, Iowa 50011, USA*
[2]*Department of Aerospace Engineering, Iowa State University, Ames, Iowa 50011, USA*
[3]*Department of Material Science and Engineering, Iowa State University, Ames, Iowa 50011, USA*
(Received 7 May 2010; revised manuscript received 15 October 2010; published 23 November 2010)

Strain-induced phase transformations (PTs) under high-pressure differ fundamentally from the pressure-induced PTs under quasihydrostatic conditions. A model and finite-element approach to strain-induced PTs under compression and torsion of a sample in rotational diamond anvil cell are developed. The current paper is devoted to the numerical study of strain-induced PTs under compression in traditional diamond anvils while the accompanying paper [V. I. Levitas and O. M. Zarechnyy, Phys. Rev. B **82**, 174124 (2010)] is concerned with compression and torsion in rotational anvils. Very heterogeneous fields of stress tensor, accumulated plastic strain, and concentration of the high-pressure phase are determined for three ratios of yield strengths of low-pressure and high-pressure phases. PT kinetics depends drastically on the yield strengths ratios. For a stronger high-pressure phase, an increase in strength during PT increases pressure and promotes PT, serving as a positive mechanochemical feedback; however, maximum pressure in a sample is much larger than required for PT. For a weaker high-pressure phase, strong strain and high-pressure phase localization and irregular stress fields are obtained. Various experimentally observed effects are reproduced and interpreted. Obtained results revealed difficulties in experimental characterization of strain-induced PTs and suggested some ways to overcome them.

DOI: 10.1103/PhysRevB.82.174123 PACS number(s): 64.60.−i, 64.70.K−, 46.35.+z

I. INTRODUCTION

Phase transformations (PTs) and chemical reactions under high pressure and large plastic shear deformation play important roles in various technical, physical, and natural processes. As examples, we can mention syntheses of materials using mechanical activation and alloying;[1,2] shear ignition of energetic and explosive materials, particularly in shear bands;[3,4] PT during the extrusion process; initiation of earthquake via PT in shear band;[5] and high-pressure search for new phases and reactions. Other examples include processes during penetration in various materials, such as armor ceramics and geomaterials, and during cutting and polishing of semiconducting and ceramics materials (such as Si, Ge, and SiC). All of these processes can be considered under the umbrella of high-pressure mechanochemistry.[6–8] One can also mention mechanochemically enhanced PTs under nanoindentation,[9] plastic-strain-enhanced reactions in rocks,[10] and mechanically induced change in reaction pathways in polymers.[11]

Pioneering studies on the unique mechanochemical behavior of materials under high pressure and large plastic strains have been initiated using rotational Bridgman anvils.[12–14] The sample was compressed to high pressure by two anvils made of hard alloys and then plastic shear was superposed by rotation of one of the anvils. Qualitative progress was made when the rotational diamond anvil cell was developed and utilized for the same type of experiments[15–19] [see Fig. 1(a)]. Use of transparent diamond allowed the measurement *in situ* of the pressure distribution (by measuring fluorescence of distributed ruby particles) and tracking of the position of the interface between phases, provided there is a color change during the PTs.[15–23]

It was found that the superposition of plastic shear under constant compressive load, due to the rotation of an anvil, leads to findings that have both fundamental and applied importance.[7,8,15–20] They are enumerated below and reviewed in detail in Refs. 7 and 8. (1) Plastic shear leads to a significant (in some cases by a factor of 3–5) reduction in PT and

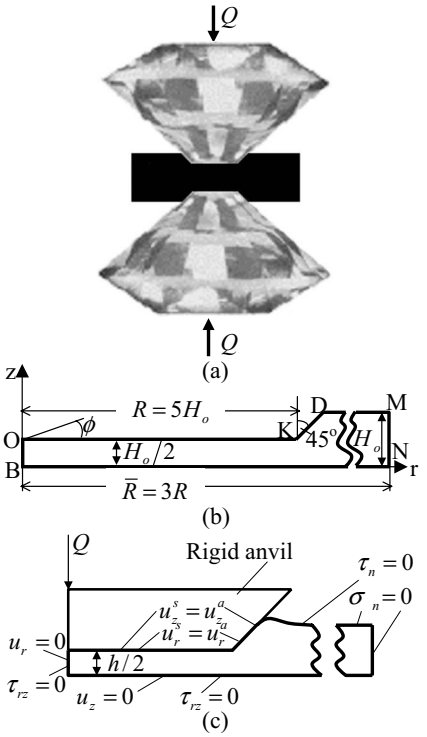

FIG. 1. (a) Schematics of rotational diamond anvil cell, (b) schematics of a sample, and (c) boundary conditions.

chemical reaction pressure. (2) It also leads to the formation of new phases that were not produced without shear. (3) The volume fraction of the high-pressure phase or the reaction product is an increasing function of the plastic shear strain. Therefore, strain-controlled (rather than time-controlled) kinetics is considered. (4) Plastic shear reduces pressure hysteresis, i.e., the difference between the start pressure of direct and reverse PT, in some cases to zero. From this, it was claimed that the obtained PT pressure can be interpreted as an equilibrium pressure.[15] (5) In some cases, shear deformation substitutes a reversible PT for an irreversible PT. Consequently, it allows production of phases that are metastable at normal pressure and that can be used in engineering applications. Results (1) and (4) have a preliminary character because they are obtained from complex experimental data that are not understood due to a lack of theory and simulations.

While most of our results below may be equally applicable to both PTs and chemical reactions,[7,8] we will focus on PTs here. It was recently recognized that strain-induced PTs differ fundamentally from the similar pressure-induced PTs.[7,8,24] Pressure- and stress-induced PTs start predominantly at pre-existing defects (various dislocation configurations and internal boundaries) at stress levels below the yield strength. It is necessary to increase pressure to drive the PTs further. Strain-induced PTs occur by nucleation at new defects permanently generated during plastic flow. As steady supply of nucleation cites precludes saturation in PT kinetics and the necessity to increase pressure. Moreover, because new defects may be stronger (i.e., produce stronger stress concentration) than the pre-existing ones, external pressure to drive the PTs can be reduced. Physics, mechanisms, thermodynamics, and kinetics of strain-induced PTs are completely different from those for pressure-induced PTs. For strain-induced PTs, phase equilibrium pressure is not a relevant parameter, and the concept of PT pressure is not well defined because it depends upon plastic strain and the concentration c of the high-pressure phase. Mechanochemistry under compression and shear is a truly multiscale phenomenon. Our nanoscale and microscale theory[7,8,24] suggests that strain-induced PTs can be characterized in terms of pressure-dependent, strain-controlled kinetics, in which time does not play any role and strain is a timelike parameter. However, PT kinetics can be experimentally determined in a macroscopic sample only. This was not done yet for several reasons. First, the fields of stress and strain tensors and concentration of the high-pressure phase are extremely heterogeneous; they strongly vary and interact with each other during loading leading to PTs. Second, these variations and interactions could not be measured. In "old" experiments, pressure was estimated as force over area of a sample,[12–14] and the concentration of high-pressure phase averaged over the sample was evaluated in the recovered sample. Due to heterogeneity of all fields, the results of these studies have a qualitative character. In more recent tests,[15–20] pressure distribution is measured. PT is qualitatively identified by a change in color, electric conductivity, or steps on pressure distribution, as well as by analysis of the sample after unloading. Recently,[20–23] we conducted *in situ* x-ray diffraction measurement with synchrotron radiation for PT in boron nitride (BN), which allowed us to determine distribution along the radius of concentration of the high-pressure phase averaged over the sample thickness. However, without knowledge of the distribution of plastic strain over the sample and the concentration of product phase and pressure over the sample thickness, which currently cannot be measured, it is impossible to quantitatively characterize and study strain-induced PTs.

The main way how the effect of shear was estimated was to compare pressure, when the first portion of the high-pressure phase appears under condition of compression without torsion and with torsion. Alternatively, pressure at the plateau of the pressure distribution, which corresponds to a diffuse interface, was compared before and after rotation of an anvil. This pressure was interpreted as PT or phase-equilibrium pressure.[15–19] It was assumed that the plateau corresponds a two-phase zone between a completely transformed high-pressure phase at the central part of a sample and a low-pressure phase. However, the nature of these plateaus, as well as the meaning of these pressures for PT characterization, is not yet clear.

It is believed in the literature that one produces pressure-induced PTs under "quasihydrostatic" conditions during compression without torsion. However, if there is irreversible change in sample thickness, beyond compaction (i.e., increase in density) for powder material, then there is plastic flow and strain-induced PTs under compression without torsion as well. Thus, there is no fundamental difference between PTs under compression without and with torsion; it is just a difference in the pressure-plastic strain path for these experiments.[7,8] This implies that we need to study strain-induced PTs under both conditions, compare results, and then draw conclusions about the effects of plastic strain on PTs.

Thus, without knowledge of the distribution of stress and plastic strain tensors over the samples and the concentration of high-pressure phase over the sample thickness, which currently cannot be measured, it is impossible to quantitatively characterize and study strain-induced PTs under compression and compression and torsion. Currently, modeling and numerical simulation is the only way to determine all fields, to understand main regularities of their variation and interaction, and to check the current hypothesis. Because physical and kinetics parameters are unknown, we need to develop an iterative, numerical-experimental procedure to extract material properties and PT kinetics. The problem of the plastic flow of material compressed in Bridgman or diamond anvil cell was studied in Refs. 25–31 using the finite-element method (FEM) and in Ref. 32 using slip-line method. The only work devoted to the FEM study of plastic flow in rotational diamond anvil cell but *without PTs* is Ref. 31.

There are few works devoted to the study of PT under compression in diamond anvil cell and rotational diamond anvil cell using a simplified analytical approach. In Refs. 33–35 initiation of PT in rotational diamond anvil cell were studied semiqualitatively. While pressure-induced PTs were considered, some predictions on the effects of PT and rotation of an anvil on plastic flow were reasonable. Thus reduction in the sample thickness during rotation of an anvil was predicted and later confirmed experimentally in Refs. 19 and 20. Also, the pressure self-multiplication effect during rota-

tion of an anvil was explained. However, other predictions are not confirmed by the current detailed FEM study. In Ref. 36, pressure-induced PT in a plane layer was studied under compression. An oversimplified PT criterion (pressure is equal to phase equilibrium pressure at the interface boundary), combined with another unrealistic assumption that the yield strength in the two-phase region during PT tends to zero (see discussion in Refs. 7 and 8), were used to reproduce a plateau at pressure distribution. In Ref. 37, the theory for pressure-induced PT was used to explain low-pressure PT in BN and to predict the phenomenon of PT induced by rotational plastic instability. In Refs. 38 and 39, FEM simulations were performed for pressure-induced PT under compression using our theory[40–42] and numerical algorithms.[41,43]

The only work in which a semiqualitative analysis of strain-induced PTs within a simplified model is Refs. 7 and 8. One of the basic equations for analysis of experiments in traditional and rotational diamond anvil cells in all analytical treatments is the simplified equilibrium equation[7,8]

$$dp/dr = -2\tau_{rz}(h/2)/h, \tag{1}$$

where dp/dr is the radial pressure gradient, h is the sample thickness, and $\tau_{rz}(h/2)$ is the radial shear (friction) stress at the contact surface between diamond and sample. It follows from Eq. (1) that a zero pressure gradient at the plateau of the pressure distribution leads to $\tau_{rz}(h/2)=0$. Consequently, either the yield strength in the plateau region should be zero (which was assumed in Ref. 36) during the PT or the radial velocity can be zero (due to a volume decrease during PT). Alternatively, semiqualitative models may lead to significant (up to zero) reduction in radial shear stresses (and consequently pressure gradient) due to the transformation-induced plasticity phenomenon, as was suggested in Refs. 7 and 8).

In this paper, we formulate a model, develop a numerical approach, and study the main features of coupled plastic flow and strain-induced PTs and chemical reactions under compression in diamond anvil cell. The same model and approach are applied in Ref. 44 to study processes under compression and torsion in rotational diamond anvil cell. The strain-controlled kinetic Eq. (17) used in this study was derived in our papers[7,8,24] based on nanoscale and microscale analysis of strain-induced PTs. Two characteristic pressures p in PT kinetic Eq. (17) are of special importance: the minimum pressure p_ε^d below which direct strain-induced PT is impossible and the maximum pressure p_ε^r above which reverse strain-induced PT is impossible. Very nonuniform fields of stress, strain, and plastic strain tensors, accumulated plastic strain q (the Odqvist parameter) and concentration of the high-pressure phase c are determined for three ratios of the yield strengths of low-pressure σ_{y1} and high-pressure σ_{y2} phases ($\sigma_{y1}=\sigma_{y2}$, $\sigma_{y1}=0.2\sigma_{y2}$, and $\sigma_{y1}=5\sigma_{y2}$, where the subscripts 1 and 2 are for low-pressure and high-pressure phases). Various experimentally observed effects are reproduced and interpreted. When high-pressure phase is weaker than the low-pressure phase, a simplified Eq. (1) is not applicable and leads to a wrong interpretation of experiments and intuition in the field. Only for this case, the experimentally observed plateau on pressure distribution was reproduced in simulations. However, it does not correspond to any characteristic pressure and is determined by the mechanics of plastic flow with PT rather than some specific characteristic of PT. On the other hand, for all cases and for any compression stage, at the point of the contact surface, where concentration of the high-pressure phase becomes nonzero, pressure corresponds to p_d^ε. This result can be used for experimental determination of p_d^ε. Since reverse PT does not occur during the compression, the characteristic pressure p_r^ε does not participate in equations and cannot be determined from a compression experiment. Some preliminary results are presented in our short letter.[33]

We designate vectors and tensors with boldface symbols and designate contractions of tensors $\boldsymbol{A}=\{A_{ij}\}$ and $\boldsymbol{B}=\{B_{ji}\}$ as $\boldsymbol{A}\cdot\boldsymbol{B}=\{A_{ij}B_{jk}\}$. Subscripts s and a denote the symmetric and skew-symmetric parts of a tensor, and $\boldsymbol{I}$ is the unit tensor.

II. THEORY AND SPECIFIC MODEL FOR STRAIN-INDUCED PHASE TRANSFORMATIONS

The deformation of a body is described by the unambiguous and differentiable vector function $\boldsymbol{r}=\boldsymbol{r}(\boldsymbol{r}_0,t)$, where $\boldsymbol{r}_0$ and $\boldsymbol{r}$ are the particle position vectors in the undeformed (reference) configuration and in the deformed (current) configuration at time t. The deformation gradient, $\boldsymbol{F}=\partial\boldsymbol{r}/\partial\boldsymbol{r}_0$, determines particle deformation and rigid-body rotation. For large strains, the multiplicative decomposition of the deformation gradient $\boldsymbol{F}=\boldsymbol{F}_e\cdot\bar{\boldsymbol{F}}_t\cdot\bar{\boldsymbol{F}}_p$ into elastic $\boldsymbol{F}_e$, transformational $\bar{\boldsymbol{F}}_t$, and plastic $\bar{\boldsymbol{F}}_p$ contributions is applied.[40] It is convenient to rearrange Eq. (2) by decomposing $\boldsymbol{F}_e=\boldsymbol{V}_e\cdot\boldsymbol{R}$ into the symmetric elastic stretch tensor $\boldsymbol{V}_e$ and the orthogonal rigid-body rotation tensor $\boldsymbol{R}$. Then,

$$\boldsymbol{F}=\boldsymbol{V}_e\cdot\boldsymbol{F}_t\cdot\boldsymbol{F}_p=\boldsymbol{V}_e\cdot\boldsymbol{F}_i,\quad \boldsymbol{F}_i:=\boldsymbol{F}_t\cdot\boldsymbol{F}_p. \tag{2}$$

Here, $\boldsymbol{F}_p=\boldsymbol{R}\cdot\bar{\boldsymbol{F}}_p$ is the rotated plastic deformation gradient tensor, $\boldsymbol{F}_t=\boldsymbol{R}\cdot\bar{\boldsymbol{F}}_t$ is the transformation deformation gradient tensor, and $\boldsymbol{F}_i$ is the inelastic deformation gradient. The introduction of $\boldsymbol{F}_i$ allows us to directly use some kinematic results from Ref. 32.

We introduce elastic deformation measures $\boldsymbol{C}_e=\boldsymbol{V}_e\cdot\boldsymbol{V}_e$ and $\boldsymbol{B}_e=0.5(\boldsymbol{C}_e-\boldsymbol{I})$, inelastic deformation rate $\boldsymbol{d}_i=(\dot{\boldsymbol{F}}_i\cdot\boldsymbol{F}_i^{-1})_s=(\dot{\boldsymbol{F}}_t\cdot\boldsymbol{F}_t^{-1})_s+(\boldsymbol{F}_t\cdot\dot{\boldsymbol{F}}_t\cdot\boldsymbol{F}_p^{-1}\cdot\boldsymbol{F}_p^{-1})_s=\boldsymbol{d}_t+\boldsymbol{d}_p$, and the skew-symmetric spin tensor $\boldsymbol{W}=(\dot{\boldsymbol{F}}\cdot\boldsymbol{F}^{-1})_a$, where $\boldsymbol{d}_t$ and $\boldsymbol{d}_p$ are the transformational and plastic parts of the deformation rate. Then, the total system of equations includes:[8,24,32,40]

decomposition of deformation rate $\boldsymbol{d}=(\dot{\boldsymbol{F}}\cdot\boldsymbol{F}^{-1})_s$ into elastic and inelastic parts:[32]

$$\overset{\nabla}{\boldsymbol{d}}=\dot{\boldsymbol{B}}_e-2(\boldsymbol{d}\cdot\boldsymbol{B}_e)_s+\boldsymbol{C}_e\cdot\boldsymbol{d}_i. \tag{3}$$

Elasticity law:

$$\boldsymbol{T}=\rho\boldsymbol{V}_e\cdot\frac{\partial\psi}{\partial\boldsymbol{B}_e}\cdot\boldsymbol{V}_e. \tag{4}$$

Yield condition and plastic flow rule:

$$\varphi(\boldsymbol{T},q,c)\le 0,\quad \boldsymbol{d}_p=\boldsymbol{f}(\boldsymbol{T},d,c). \tag{5}$$

Evolution of transformational deformation gradient:

$$\boldsymbol{F}_t = \tilde{f}(\boldsymbol{T}, c). \tag{6}$$

Strain-controlled kinetic equation:

$$\frac{dc}{dq} = f(\boldsymbol{T}, q, c). \tag{7}$$

Momentum balance equation:

$$\boldsymbol{\nabla} \cdot \boldsymbol{T} = \rho \ddot{\boldsymbol{r}}. \tag{8}$$

Here, $\overset{\nabla}{\boldsymbol{B}}_e = \dot{\boldsymbol{B}}_e + 2(\boldsymbol{B}_e \cdot \boldsymbol{W})_s$ is the objective Jaumann time derivative; $\boldsymbol{T}$ is the true Cauchy stress tensor; ρ is the mass density in the deformed configuration; ψ is the elastic potential (e.g., the Helmholtz free energy) per unit mass; q is the accumulated plastic strain $[\dot{q} := (2/3\boldsymbol{d}_p : \boldsymbol{d}_p)^{1/2}]$; c is the concentration of the high-pressure phase defined as the ratio of the undeformed volumes of the high-pressure phase and two-phase mixture; f, $\tilde{f}$, and $\boldsymbol{f}$ are constitutive functions to be determined; and $\boldsymbol{\nabla}$ is the gradient operator in the deformed configuration.

To obtain the first generic results, we will consider the simplest model for both plasticity and PT. Thus, for plasticity, the simplest isotropic, perfectly plastic model will be used, which is described, for example, in Ref. 32. Without PTs, the perfectly plastic and isotropic model is justified for various classes of materials (metals, rocks, pressed powders, etc.) for large strains $q > 0.6 \div 1$. Decomposing $\boldsymbol{V}_e = \boldsymbol{I} + \boldsymbol{\varepsilon}_e$ and $\boldsymbol{F}_t = \boldsymbol{I} + \boldsymbol{\varepsilon}_t$, we will limit ourselves to the simplest case of small elastic strain $\boldsymbol{\varepsilon}_e \ll \boldsymbol{I}$ and small and pure volumetric transformation strain $\boldsymbol{\varepsilon}_t = \varepsilon_t \boldsymbol{I}$, $\varepsilon_t \ll 1$. This means, in particular, that we neglect transformation- and reaction-induced plasticity, which produces a deviatoric contribution to $\boldsymbol{F}_t$. Under such assumptions, we have the following simplifications in Eqs. (3) and (4): $\boldsymbol{V}_e \simeq \boldsymbol{C}_e \simeq \boldsymbol{I}$, $\boldsymbol{B}_e \simeq \boldsymbol{\varepsilon}_e$, $(\boldsymbol{d} \cdot \boldsymbol{B}_e)_s \simeq 0$, $\boldsymbol{d}_t = \dot{\varepsilon}_t \boldsymbol{I}$, and $\boldsymbol{d}_p = (\dot{\boldsymbol{F}}_p \cdot \boldsymbol{F}_p^{-1})_s$. Then, the total system of equations includes:

kinematic decomposition:

$$\boldsymbol{d} = (\dot{\boldsymbol{F}} \cdot \boldsymbol{F}^{-1})_s = \overset{\nabla}{\boldsymbol{\varepsilon}}_e + \dot{\varepsilon}_t \boldsymbol{I} + \boldsymbol{d}_p. \tag{9}$$

Hooke's elasticity rule:

$$p = K\varepsilon_{e0}, \quad \boldsymbol{s} = 2G \ dev\boldsymbol{\varepsilon}_e. \tag{10}$$

Von Mises yield condition:

$$\sigma_i \leq \sigma_y(c), \quad \sigma_y := (1-c)\sigma_{y1} + c\sigma_{y2}. \tag{11}$$

Associated plastic flow rule:

in the elastic regime:

$$\sigma_i < \sigma_y(c), \quad \boldsymbol{d}_p = 0. \tag{12}$$

In the plastic regime:

$$\sigma_i = \sigma_y(c), \quad \boldsymbol{d}_p = \lambda \boldsymbol{s}. \tag{13}$$

Consistency condition:

$$\dot{\sigma}_i = \dot{\sigma}_y \Rightarrow \lambda = \frac{3}{2}\frac{\boldsymbol{s}:\boldsymbol{d}}{\sigma_y^2} - \frac{(\sigma_{y2} - \sigma_{y1})\dot{c}}{\sigma_y G}. \tag{14}$$

Transformation strain:

$$\varepsilon_t = \bar{\varepsilon}_t c. \tag{15}$$

Equilibrium equation:

$$\boldsymbol{\nabla} \cdot \boldsymbol{T} = 0. \tag{16}$$

Strain-controlled kinetics of phase transformations are:

$$\frac{dc}{dq} = \frac{\frac{(1-c)}{a_{12}}\bar{p}_d H(\bar{p}_d)\frac{\sigma_{y2}}{\sigma_{y1}} - \frac{c}{a_{21}}\bar{p}_r H(\bar{p}_r)}{c + (1-c)\sigma_{y2}/\sigma_{y1}}, \tag{17}$$

$$\bar{p}_d = \frac{p - p_\varepsilon^d}{p_h^d - p_\varepsilon^d}, \quad \bar{p}_r = \frac{p - p_\varepsilon^r}{p_h^r - p_\varepsilon^r}. \tag{18}$$

Here, K and G are the bulk and shear moduli, assumed to be the same for both phases; dev is the deviatoric operator; $\boldsymbol{s} = dev\boldsymbol{T}$ is the deviatoric stress part of the Cauchy stress; ε_{e0} is the volumetric elastic strain; $\sigma_i = (3/2\boldsymbol{s}:\boldsymbol{s})^{1/2}$ is the stress intensity; Eq. (11) is the linear approximation for the yield strength σ_y of a two-phase mixture in terms of the yield strengths of the low- and high-pressure phases σ_{y1} and σ_{y2}, respectively; and $\bar{\varepsilon}_t$ is the volumetric transformation strain during PT. The consistency condition, Eq. (14), means that the yield condition is satisfied not at time t only but at time $t + \Delta t$ as well; it allows determination of the scalar λ. Equation (17) is a particular case of the strain-controlled kinetic equations from Refs. 7, 8, and 24 for PTs between two phases, a_{ij} are the kinetic parameters, H is the Heaviside step function, p_h^d and p_h^r are the pressures for direct and reverse PTs under hydrostatic conditions, p_ε^d is the minimum pressure below which direct strain-induced PT is impossible, and p_ε^r is the maximum pressure above which reverse strain-induced PT is impossible.

Equation (14) for λ is derived as follows. Differentiating the Hooke's law in Eq. (10), $\overset{\nabla}{\boldsymbol{s}} = 2G dev \overset{\nabla}{\boldsymbol{\varepsilon}}_e$, and expressing $dev\overset{\nabla}{\boldsymbol{\varepsilon}}_e$ from kinematic decomposition, Eq. (9), and flow rule Eq. (13), we obtains $\overset{\nabla}{\boldsymbol{s}} = 2G(dev\boldsymbol{d} - \boldsymbol{d}_p) = 2G(dev\boldsymbol{d} - \lambda \boldsymbol{s})$. Then, substituting this expression in the time derivative of squared Eq. (13), $\frac{3}{2}\boldsymbol{s}:\overset{\nabla}{\boldsymbol{s}} = \frac{d\sigma_y^2}{dc}\dot{c}$, and solving for λ, we obtain Eq. (14).

III. PROBLEM FORMULATION

The schematics of rotational diamond anvil cell is shown in Fig. 1(a). Since the anvil contains 8, 16, 24, or 32 facets, it is approximated by a cone. Axisymmetric geometry and problem formulation in a cylindrical coordinate system $rz\phi$ are used. Here, we will focus on the compression stage without torsion, and thus loading is also axisymmetric. Due to symmetry with respect to the plane $z=0$ passing through the center of a sample, a quarter of a cross section of a sample before deformation is shown in Fig. 1(b). The initial thickness of a sample between the flat diamond surface $H_0 = 0.2R$, where R is the anvil radius; the initial thickness of the free part of the sample $H = 2H_0$. To avoid any influence of the edge of the sample, the external radius of the sample is chosen as $3R$.

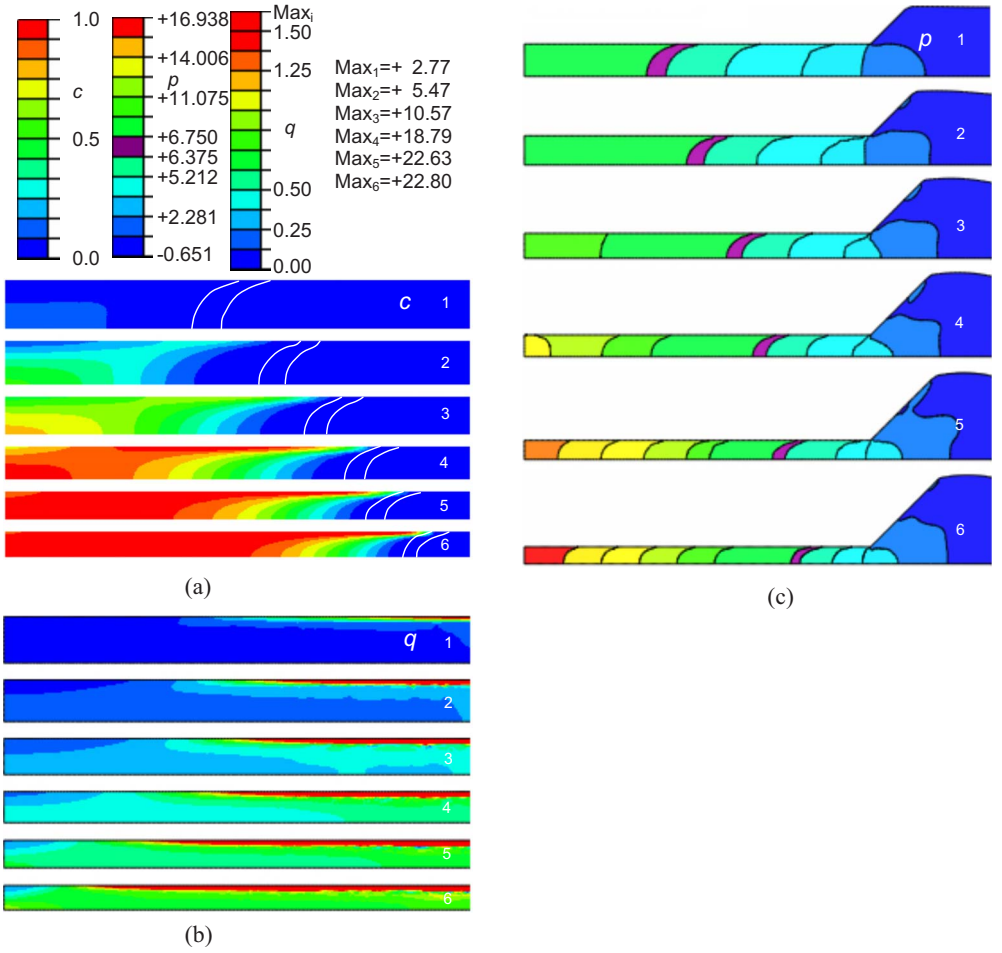

FIG. 2. (Color online) (a) Distribution of the concentration of high-pressure phase c, (b) accumulated plastic strain q, and (c) pressure p for the case with $\sigma_{y2}=\sigma_{y1}$ for different values of the dimensionless applied axial force F in a quarter of cross section of the sample. Pressure range $p_\varepsilon^r<p<p_\varepsilon^d$ is shown in magenta. The contours of this region are duplicated in Fig. 2(a) for concentration, similar to all other figures with concentration fields in a sample. Maximum values of accumulated plastic strain q for each of six compression stages are shown near color legend. The same is shown in all other figures with pressure and accumulated plastic strain fields in a sample. 1: $F=4.29$, 2: $F=4.83$, 3: $F=5.50$, 4: $F=6.09$, 5: $F=6.73$, and 6: $F=7.44$.

Initial conditions represent zero value of all stresses, strains, concentration of high-pressure phase, and displacements. The following boundary conditions are applied [Fig. 1(c)]: (1) at the axis OB ($r=0$), the radial shear stress $\tau_{zr}=0$, and the radial displacement $u_r=0$. (2) At the plane of symmetry BC $z=0$, $\tau_{zr}=0$, and the axial displacements $u_z=0$. (3) At the deformed free surfaces DM and MN, the components of the traction $\sigma_n=\tau_n=0$.

(4) At the contact surface OKD between rigid diamond and compressed material, compressive force Q increasing from zero to final value was applied to the rigid surface that models diamond. Using rigid surface OKD results in the condition that u_z is the same for each point of contact surface. Also, radial displacement $u_r=0$, i.e., the complete cohesion condition was used. As will be demonstrated, this condition results in the maximum possible shear stress $\tau_{rz}=\tau_y$ at the most part of the flat contact surface and the smooth reduction in τ_{rz} to zero near the rotation axis, as is expected from experiments on compression of thin disk. The large elastoplastic deformation and coupled thermomechanical subroutines of the FEM code ABAQUS were implemented, in which the transformation strain was modeled through the thermal strain. Concentration c was treated as the temperature and thermal conduction equation with zero thermal conductivity, and heat sources according to Eq. (17) were used to solve kinetic Eq. (17). The loading path was divided into a number of steps and after each step the ABAQUS built-in remeshing procedure was performed.

All parameters with dimension of stress are normalized by the yield strength in compression of the low-pressure phase σ_{y1}, e.g., $\bar{\sigma}_{rr}=\sigma_{rr}/\sigma_{y1}$ and $\bar{p}=p/\sigma_{y1}$. Dimensionless applied axial force is defined as $F=Q/(S\sigma_{y1})$, with S for the initial contact area OKD between an anvil and a sample with gasket. For convenience, in figures shear stresses are divided by the yield strength in shear $\tau_{y1}=\sigma_{y1}/\sqrt{3}$, e.g., $\bar{\tau}_{rz}=\tau_{rz}/\tau_{y1}$.

Compressive normal stresses and strains will be considered as positive ones. The following dimensionless material parameters were utilized in calculations: $\bar{\varepsilon}_t=0.1$, Young's modulus $E=162.5$, Poison's ratio $\nu=0.3$, $p_\varepsilon^d=6.75$, $p_\varepsilon^r=6.375$, $p_h^d=11.25$, $p_h^r=1.875$, and $a_{ij}=0.1$. Note that contour lines of equal values of the normal stresses σ_{zz} and σ_{rr}, and shear stresses τ_{rz}, as well as distributions of the normal

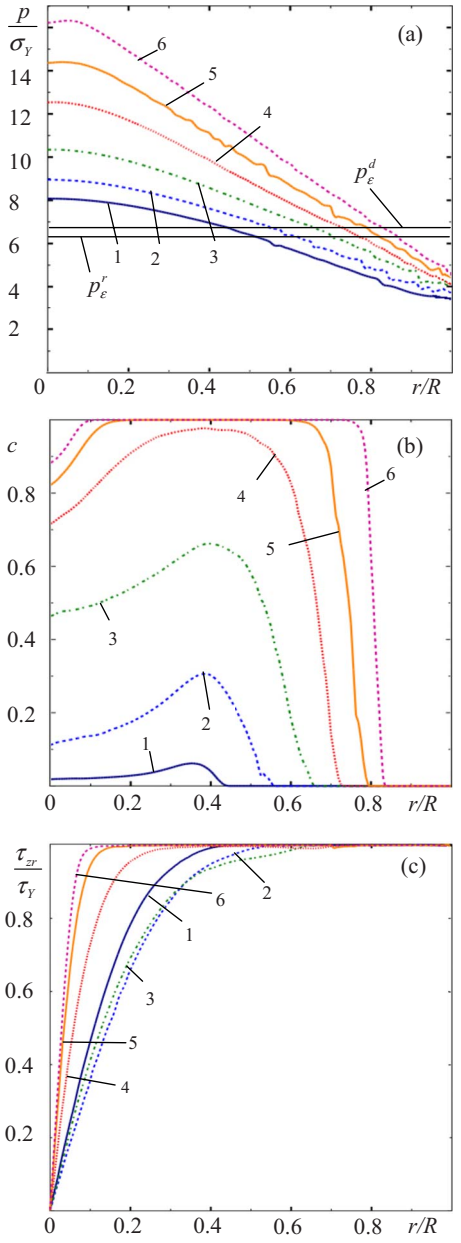

FIG. 3. (Color online) (a) Distribution of pressure p, (b) concentration of high-pressure phase c, and (c) shear stress τ_{zr} along the radius of the contact surface of a sample r for the case with $\sigma_{2y}=\sigma_{1y}$ for different values of the dimensionless applied axial force F in a quarter of cross section of the sample. 1: $F=4.29$, 2: $F=4.83$, 3: $F=5.50$, 4: $F=6.09$, 5: $F=6.73$, and 6: $F=7.44$.

stresses σ_{zz} and σ_{rr} along the flat contact surface between the sample and the anvil are presented in supplementary material.[45]

IV. PHASE TRANSFORMATIONS FOR EQUAL YIELD STRENGTH OF PHASES

We will discuss the PTs for $\sigma_{y1}=\sigma_{y2}$ and six values of applied force F. Distributions for smaller applied force before PTs can be found in Ref. 31. Plastic strain appears first near the corner $r=R$ and $z=h$ of the anvil-sample contact surface [Fig. 2(b)]. With an increase in F, it propagates predominantly along the contact surface in the direction toward the center of the sample. When F increases from 4.18 to 5.91, the maximum value of q grows from 2.77 to 22.80. While q is much higher at the surface of the sample than its value in the middle of the sample, PT does not start until pressure reaches a minimum pressure p_ε^d for direct PT.

With increasing axial force, an almost linear growth of the pressure along the radius is observed at the major part of the contact surface [Figs. 2(c) and 3(a)], with a slow parabolic growth at the central part of the sample, similar to the case without PT.[31] No effect of PT (like a pressure plateau in the area of phase interface) can be seen. Pressure reduces from the contact surface to the symmetry plane for the same r and pressure contour lines look parabolic. In Fig. 2(c), the pressure range $p_\varepsilon^r<p<p_\varepsilon^d$ is shown in magenta, similar to all other figures with pressure fields in a sample. This is a region, where neither direct nor reverse PTs are possible. In the region with higher pressure (to the left of the magenta region) direct PT is possible; in the region with lower pressure (to the right) reverse PT is possible, provided that a high-pressure phase exists in it. The contours of this region are duplicated in Fig. 2(a) for concentration, similar to all other figures with concentration fields in a sample. Under compression, pressure grows faster than PT progresses, and therefore reverse PT never takes place for any ratio σ_{y2}/σ_{y1}, in contrast to the case of torsion under pressure. The PT starts at the center of the sample [Figs. 2(a) and 3(b)], where pressure is close to maximum value in a sample and plastic strain is concentrated along the slip line. High-pressure phase propagates in the radial direction and toward the surface of the sample. Another local maximum in c appears along the contact surface in the region with very large q but lower p. Then those areas merge into one and progress further. With proper increase in the pressure, it is possible to transform the whole sample. The above heterogeneous concentration distribution means that when, in experiments with transparent low-pressure phase and opaque high-pressure phase (e.g., for KCl), we observes the opaque area, it does not mean that PT in it is completed. In the given example, PT completes in some disklike area of a sample at stage 5 only. Note, that complete PT occurs at maximum pressure at the center that is more than two times p_d^ε. This means that compression is not an effective way to produce strain-induced PT at low pressure.

While pressure distribution does not change appreciably due to PT, for any compression stage, pressure at the contact surface at the point where PT starts, corresponds to the characteristic pressure p_d^ε [Fig. 3(a)]. This result maybe used to determine p_d^ε in an experiment.

Shear stress τ_{zr} [Fig. 3(c)] is bounded by τ_y. With an increase in the applied axial force region with $\tau_{zr}=\tau_y$ approaches the center of the sample. Without PT, this region grows monotonously with increasing force. With PT, there is some reduction in this region between steps 1 and 3, after which it grows again. In this region, shear stress is practically independent of r and reduces monotonously to zero at the symmetry plane. Since plastic flow highly localizes near the contact surface in the region with maximum possible shear stresses, it simulates relative sliding of the material

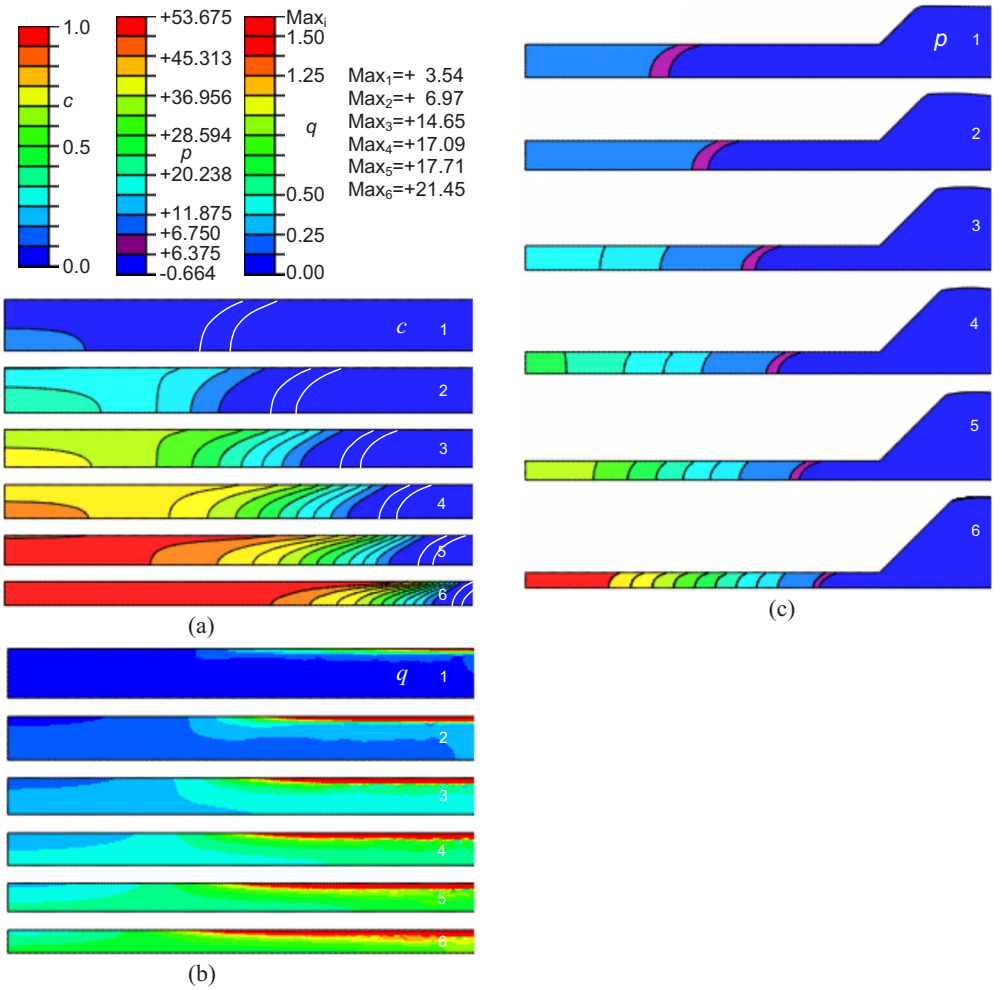

FIG. 4. (Color online) (a) Distribution of the concentration of high-pressure phase c, (b) accumulated plastic strain q, and (c) pressure p for the case with $\sigma_{y2}=5\sigma_{y1}$ for different values of the dimensionless applied axial force F. 1: $F=4.29$, 2: $F=5.09$, 3: $F=6.74$, 4: $F=8.39$, 5: $F=11.05$, and 6: $F=15.56$.

with respect to anvil (despite the cohesive boundary conditions).

In general, there is no qualitative difference in stress and strain fields evolution in comparisons with the case without PTs,[31] despite the volume decrease due to PTs. The concentration field of the high-pressure phase is distributed heterogeneously at the initial stage of compression and is governed by a combination of accumulated plastic strain and pressure. After completing the PT in the central part of the sample, the concentration is still very heterogeneous at the periphery. However, for any compression stage, at the contact surface $p=p_d^{\varepsilon}$ at the point where the concentration of the high-pressure phase starts to deviate from zero. Compression is not an effective way to produce strain-induced PT at low pressure because pressure grows significantly during compression and plastic deformation.

V. PHASE TRANSFORMATIONS TO A STRONGER HIGH-PRESSURE PHASE

Here, we will analyze the case of PTs for $\sigma_{y2}=5\sigma_{y1}$. It corresponds to PTs in various systems, for example, for $B1 \rightarrow B2$, PT in KCl, and for PT from low-density, graphitelike hexagonal, or rhombohedral phases of BN and carbon to high-density, cubic, or wurtzitic diamondlike, superhard phases. The evolution of plastic strain [Fig. 4(b)] for this case is qualitatively similar to that for $\sigma_{y2}=\sigma_{y1}$ for the same reduction in thickness. There is some local redistribution of plastic strain with some growth in the less transformed regions and reduction in more transformed regions. At step 6, the red zone with maximum accumulated plastic strain is more delocalized near the contact surface for $\sigma_{y2}=5\sigma_{y1}$ than for $\sigma_{y2}=\sigma_{y1}$.

After the PT starts at the center of the sample [Figs. 4(a) and 5(b)], concentration c increases almost homogeneously in the central part of the sample and the transformed region grows radially. Concentration c near the symmetry axis $r=0$ progresses faster than for $\sigma_{y2}=\sigma_{y1}$. The high-pressure phase does not flow in the region where $p<p_{\varepsilon}^{r}$, i.e., reverse PT does not occur. Pressure distribution [Figs. 4(c) and 5(a)] before PT starts is the same as for $\sigma_{y2}=\sigma_{y1}$. With initiation of PT in the central part of a sample, pressure gradient and pressure increase in that region. The increase in pressure intensifies PT, which promotes further drastic increase in pressure and pressure gradient, and growth of the transform-

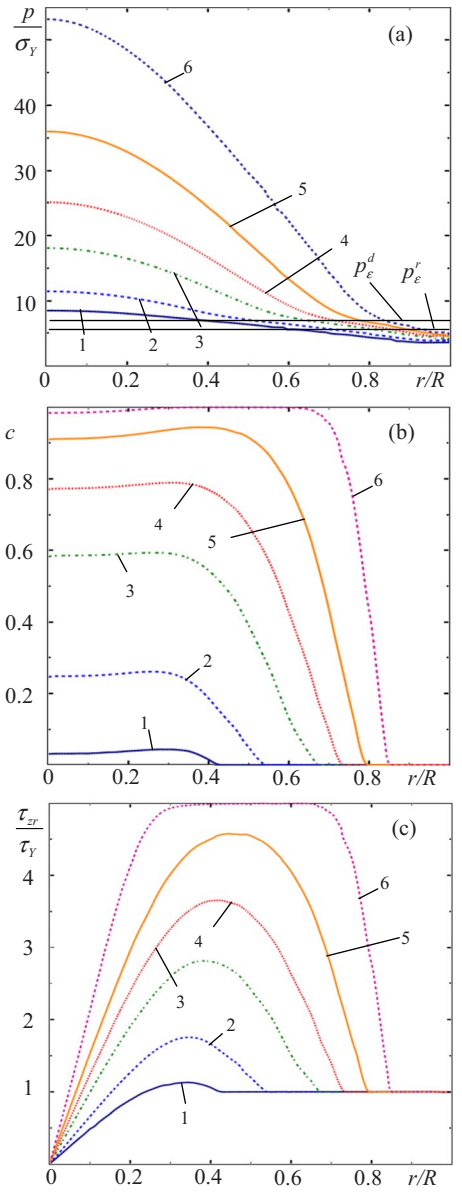

FIG. 5. (Color online) (a) Distribution of pressure p, (b) concentration of high-pressure phase c, and (c) shear stress τ_{zr} along the radius of the contact surface of a sample r for the case with $\sigma_{2y}=5\sigma_{1y}$ for different values of the dimensionless applied axial force F. 1: $F=4.29$, 2: $F=5.09$, 3: $F=6.74$, 4: $F=8.39$, 5: $F=11.05$, and 6: $F=15.56$.

ing region [Fig. 4(a)], so a positive mechanochemical feedback takes place. Also, as it follows from kinetic Eq. (17), when the reverse PT does not occur, the ratio σ_{y2}/σ_{y1} does not affect dc/dq for small c; for $c\to 1$, we have $dc/dq \sim \sigma_{y2}/\sigma_{y1}$. Thus, we would expect acceleration of PT due to a stronger high-pressure phase at relatively large c. A sharp change in pressure gradient is located in the region of diffuse interface between phases [see Figs. 5(a) and 5(b)], which became more localized with increasing force. No pressure plateau at the diffuse interface can be found. However, for any compression stage, pressure at the contact surface at the point where concentration of the high-pressure phase deviates from zero, corresponds to p_d^ε [Fig. 5(a)], similar to the case with $\sigma_{y2}=\sigma_{y1}$. This result maybe used to determine p_d^ε in an experiment.

Despite the positive feedback and increased dc/dq, compression is not an effective way to produce strain-induced strong phases at low pressure. Pressure grows drastically in the central part of a sample, where PT is completed and high pressure is not necessary at all. Thus, pressure at the center for complete PT in the central part of a sample is 36, while it is 14 for a similar transformed region for $\sigma_{y2}=\sigma_{y1}$.

Shear stress τ_{zr} at the contact surface [Figs. 5(c)] reaches τ_{y1} in the major external part of a sample before PT starts. At further loading, shear stress increases at the central part of the disk, and the region with $\tau_{zr}>\tau_{y1}$ extends toward the periphery of a sample, repeating approximately the plot $c(r)$. At step 6, when PT is completed in the major part of a sample, in some ring $\tau_{zr}=\tau_{y2}$. For this case, the region in which τ_{zr} grows from τ_{y1} to τ_{y2} coincides with the diffuse interface between phases.

To conclude this case, we found that all components of stress tensor grow in the transformed region because of the growth of the yield strength. Shear stress reaches the yield strength in shear of the high-pressure phase. Due to the pressure increase in the course of PT (positive mechanochemical feedback) and the acceleration of PT due to large σ_{y2}/σ_{y1}, according to kinetic Eq. (17) we would expect much faster PT for the same degree of compression h/h_0 than for $\sigma_{y2}=\sigma_{y1}$. In reality, due to a drastic pressure increase in the center of the sample, where PT is already completed and such pressure is useless, compression is not an effective way to produce strain-induced strong phases at low pressure. High pressure at the center may damage diamond anvils during the PT. After completing the PT in the central part of the sample, concentration is still very heterogeneous at the periphery. At the point of the contact surface where c is becoming greater than zero, we have $p=p_d^\varepsilon$ for any compression stage.

VI. PHASE TRANSFORMATIONS TO A WEAKER PHASE

We will discuss the opposite case of PT for $\sigma_{y2}=0.2\sigma_{y1}$, e.g., for PT I→II from semiconducting to metallic phases in Si and Ge, PT in ZnSe,[17] as well as PT V→VIII′ in CuI.[18] All fields for a weaker high-pressure phase are qualitatively different from the two previous cases. The main reason is that PT causes material softening and plastic flow localizes in the regions with the partially and fully transformed material [Fig. 6(b)]. Such a strain localization promotes completion of PT in localization zones but prevents spreading of transformed zones through the sample. The PT starts at the center of the sample [Figs. 6(a) and 7(b)], where pressure is close to maximum and plastic strain is concentrated along the slip line. Another local maximum in c appears along the contact surface in the region with very large plastic strain but lower pressure. These transformed regions merge into one, and plastic strain concentrates in it, leading to complete PT in a relatively narrow region. Maximum values of q in a sample are approximately the same for all three cases ($q=24.26$ for $\sigma_{y2}=0.2\sigma_{y1}$, $q=22.80$ for $\sigma_{y2}=\sigma_{y1}$, and $q=21.45$ for $\sigma_{y2}=5\sigma_{y1}$) for the similar h/h_0, because it is lo-

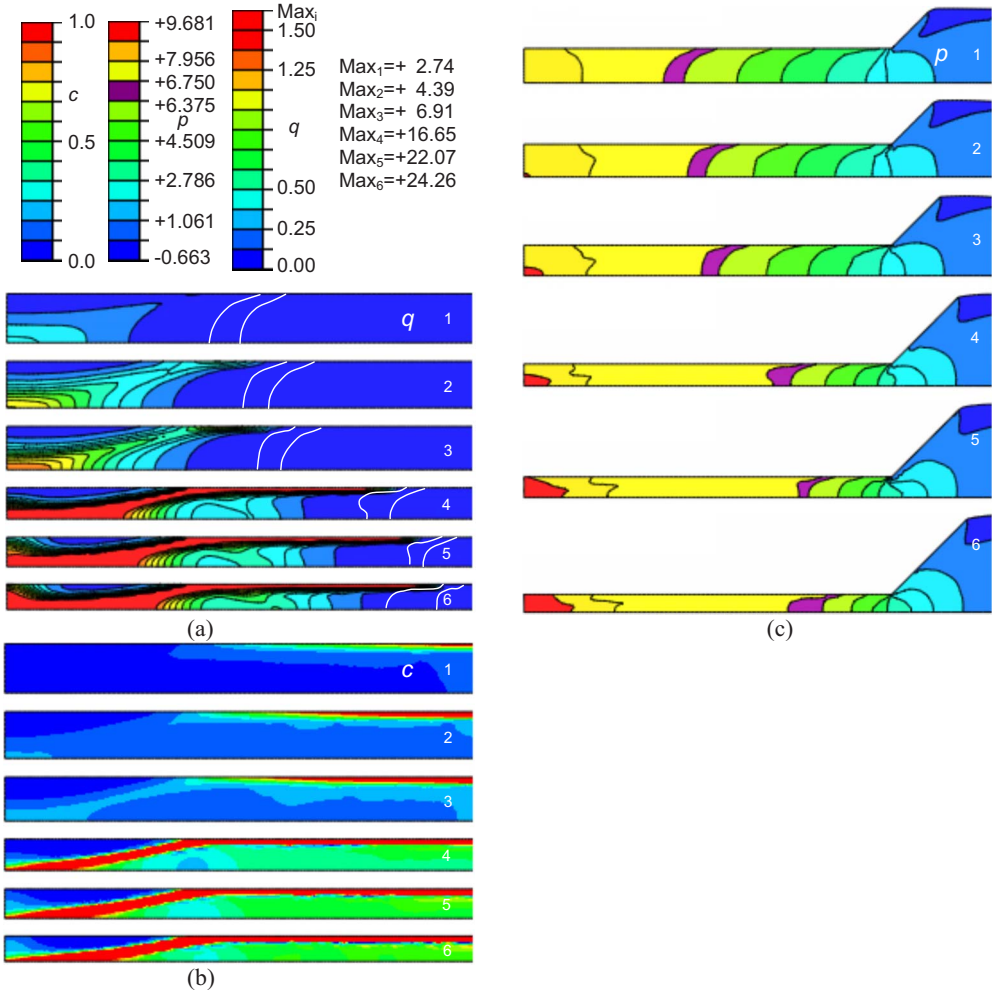

FIG. 6. (Color online) (a) Distribution of the concentration of high-pressure phase c, (b) accumulated plastic strain q, (c) pressure p for the case with $\sigma_{y2}=0.2\sigma_{y1}$ for different values of the dimensionless applied axial force F. 1: $F=4.38$, 2: $F=4.68$, 3: $F=4.80$, 4: $F=5.62$, 5: $F=5.97$, and 6: $F=6.10$.

cated near the corner point, where material is in the low-pressure phase. At the same time, the maximum value of q near the center exceeds 1.5 for $\sigma_{y2}=0.2\sigma_{y1}$, while it is two times smaller for the two other cases. Distribution of c along the contact surface [Fig. 7(b)] exhibits growth in ring $0.3 \leq r/R \leq 0.8$ and some growth near the symmetry axis with arrested PT between them.

Pressure variation at the contact surface differs from the two previous cases as well. During the first three steps, it did not change in the central part at all but increased at the periphery. During the next three steps, it slightly increased at the center and significantly at the periphery, forming a plateau in the ring where PT was completed. There is pressure deep between these regions, where PT is arrested. The plateau corresponds to the pressure range between 7.5 and 8, i.e., it is well above p_e^d. Consequently, it is determined by the mechanics of plastic flow with PT rather than by PT-related characteristics. At the same time, for any compression stage, at the point of the contact surface, where c becomes nonzero, the pressure corresponds to p_d^e [Fig. 7(a)], similar to both previous cases.

In comparison with cases $\sigma_{y2} \geq \sigma_{y1}$, pressure distribution in the sample is much more homogeneous [Fig. 6(c)]. Shear stress τ_{zr} [Fig. 7(c)] is distributed very heterogeneously. During compression, it reduces in transforming regions due to reduction in σ_y until it reaches σ_{y2} in the completely transformed region at the contact surface. Local oscillations can be seen both at the contact surface and in the bulk. While for $\sigma_{y2} \geq \sigma_{y1}$ Eq. (1) shows reasonable agreement with our FEM results, Eq. (1) is not applicable for the case with strain localization. Thus, at the plateau of p we should have $\tau_{zr}=0$ according to Eq. (1), while in simulations τ_{zr} reached its maximum possible value τ_{y2}. That is why simplified analysis based on Eq. (1) leads to incorrect conclusions and interpretations. Also, while the local minimum at the contact surface in pressure distribution in the region, where PT is arrested, corresponds to zero (or a small value) of shear stress [in agreement with Eq. (1)], shear stress does not change sign near this minimum (as does the pressure gradient), and material does not flow in the direction of the pressure gradient (i.e., to the center of the sample). This is *in contrast* to generally accepted knowledge based on Eq. (1) that the pressure maximum corresponds to zero sliding velocity and that material flows radially in the direction of the pressure gradient.[7,8,17] In addition, according to Eq. (1), the pressure gradient in the central part of the sample is expected to de-

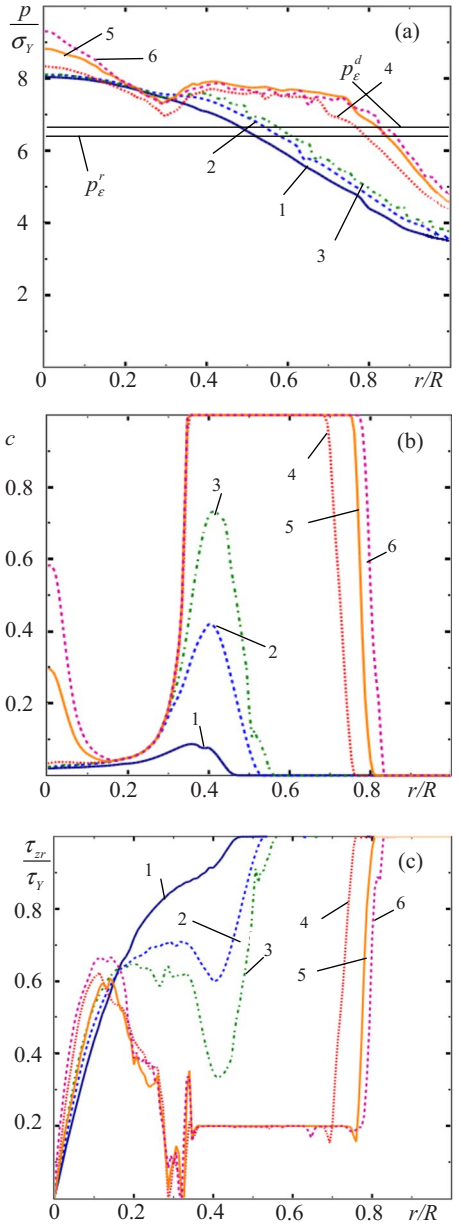

FIG. 7. (Color online) (a) Distribution of pressure p, (b) concentration of high-pressure phase c, and (c) shear stress τ_{zr} along the radius of the contact surface of a sample r for the case with $\sigma_{2y}=0.2\sigma_{1y}$ for different values of the dimensionless applied axial force F. 1: $F=4.38$, 2: $F=4.68$, 3: $F=4.80$, 4: $F=5.62$, 5: $F=5.97$, and 6: $F=6.10$.

crease due to reduction in the yield strength, but it grows.

To summarize, we conclude that due to softening during the PT, coupled strain and PT localization occurs in some narrow region. PT completes in this region but does not spread over the sample. Pressure and all stress distributions have irregular character. Plateau in the distribution of all normal stresses and pressure is observed but it does not correspond to any characteristic pressure for PT. At the same time, $p=p_d^{\varepsilon}$ for any compression stage at the point of the contact surface, where c becomes nonzero. Simplified Eq. (1) is not applicable to the case with strain localization and leads to a wrong interpretation.

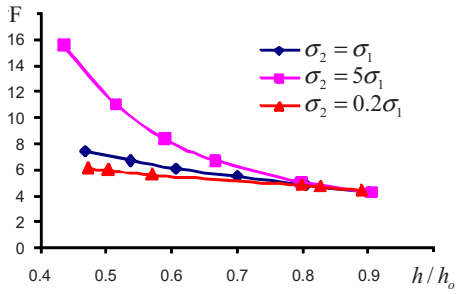

FIG. 8. (Color online) Dependence of the dimensionless applied axial force F versus relative sample thickness h/h_0.

Dependence of the force F necessary to compress the sample versus relative sample thickness h/h_0 for all cases is presented in Fig. 8. Each point corresponds to the parameters for which all plots were given in Figs. 2–7. While with the appearance of the stronger high-pressure phase force grows drastically (as would be expected), PT to a weaker phase does not reduce the force essentially. This is because pressure unexpectedly increases at the sample periphery.

VII. CONCLUDING REMARKS

To summarize, a three-dimensional model is developed, and FEM simulations of PT in diamond anvil cell are performed. The results lead to a change in the basic understanding of strain-induced PTs in terms of interpretation of experimentally observed effects and measurements and the extracting of information on material behavior from the sample behavior. They also represent a tool for designing experiments for different purposes and for controlling PTs. The following simulation results qualitatively correspond to the experiment: (a) experimentally observed plateaus [for example, for ZnSe (Ref. 17) and CuI (Ref. 18)] in the pressure-distribution curve have been reproduced for $\sigma_{y2}=0.2\sigma_{y1}$. However, our calculations for $\sigma_{y2}\geq\sigma_{y1}$ did not reproduce the plateau at the diffuse interface, which was observed in experiments for PT in KCl (Refs. 15 and 19) and fullerene.[16,19] This may be because of relatively slow kinetics, or because we considered $p_{\varepsilon}^{d}>p_{\varepsilon}^{r}$ rather than the opposite case, or because of an oversimplified model. (b) For $\sigma_{y2}\geq\sigma_{y1}$ the pressure distribution is smooth in our simulations, in accordance with a smooth, measured pressure distribution in KCl (Refs. 15 and 19) and fullerene.[16,19]

(c) The calculated pressure distribution is irregular for PT to the weaker high-pressure phase. This corresponds to an irregular pressure distribution in ZnSe (Ref. 17) and CuI.[18] At the same time, for PT from semiconducting phase I to weaker metallic phase II in Ge and Si, the pressure plot is smooth.[46,47] This may be related to involvement of PTs to and from strong semiconducting phase III, as follows from kinetic theory.[24]

(d) Simulation in Fig. 6(a) suggests that a low-strength phase should appear along the contact surface of the sample. In Ref. 48, PT from semiconducting Si I to weaker metallic Si II under compression was found in a thin contact layer only, not in the bulk. This experimental result also confirms the strain-induced (rather than pressure-induced) nature of

PT under compression without torsion: stress intensity is constant in the entire sample, pressure varies slightly along the thickness, but plastic strain is concentrated in the transformed region.

The pressure at the plateau for $\sigma_{y2}=0.2\sigma_{y1}$ does not change during the increasing load, which creates the impression that this is the PT pressure. However, this pressure does not correspond to any characteristic pressure in kinetic Eq. (17). It is determined by the mechanics of plastic flow with PT rather than some specific characteristic of PT. For all cases and for any compression stage, at the point of the contact surface, where concentration of the high-pressure phase becomes nonzero, pressure corresponds to p_d^ε. This result can be used for experimental determination of p_d^ε. The main problem is to determine such a point experimentally because concentration is distributed nonuniformly along both radius and thickness. With the x-ray diffraction methods used in Ref. 20, volume fraction is averaged over the thickness of a sample, which will not allow us to determine precisely the point at the surface where PT starts. Distribution of concentration c can be measured in the thin contact layer using Raman spectra (as for PT in Si in Ref. 48), which should give much better precision. High-resolution optical methods can also be used in cases, in which phases can be distinguished. Since reverse PT does not occur during the compression, characteristic pressure p_r^ε cannot be determined from compression experiments.

While for $\sigma_{y2}\geq\sigma_{y1}$ our results in general correspond to intuitive predictions based on a simplified Eq. (1), this equation is not applicable for the case with strain localization because of the smaller yield strength of the high-pressure phase. Thus, in the region with constant pressure shear stress is not zero but reaches its maximum τ_{y2}, shear stress does not change sign when pressure gradient does, pressure gradient does not decrease when the yield strength decreases, and material does not flow in the direction of the pressure gradient. That is why simplified analysis based on Eq. (1) leads to incorrect conclusions and interpretations.

In this paper we studied the effect of the ratio of strengths of high- and low-pressure phases on kinetics of strain-induced PT. Our conclusion may be broadened or changed when we change the kinetic coefficient or the entire equation, take $p_\varepsilon^r>p_\varepsilon^d$, and use a gasket of chosen geometry and made of different materials. Also, taking into account the pressure dependence of the mechanical properties, transformation-induced plasticity, and superposition of strain-induced and pressure-induced PT will further advance our predictive capability. Finite elastic and transformation strains will be included. In addition, continuity of displacement at the boundary between anvil and sample will be substituted with contact boundary conditions that allow slip. This is especially important when a sample is located in the hole in the gasket, because the boundary between sample, gasket, and diamond should slip along the diamond surface. Due to the strong heterogeneity of all fields, especially accumulated plastic strain and concentration of the high-pressure phase, it is difficult to extract the kinetic equation for PTs, Eq. (17), from an experiment. In Ref. 20 we predicted theoretically and confirmed experimentally the method for creating a quasihomogeneous pressure distribution in a sample by designing the sample and gasket geometry. As a result, distribution of concentration of the high-pressure phase measured by x ray (i.e., averaged over the sample thickness) was also quasihomogeneous. An FEM study of this problem will be performed in the future.

ACKNOWLEDGMENTS

ARO (Grant No. W911NF-09-1-0001), DTRA (Grant No. HDTRA1-09-1-0034), ISU, and TTU support for this research is gratefully acknowledged.

*vlevitas@iastate.edu

[1] C. C. Koch, Nanostruct. Mater. **2**, 109 (1993).
[2] L. Takacs, Prog. Mater. Sci. **47**, 355 (2002).
[3] V. I. Levitas, V. F. Nesterenko, and M. A. Meyers, Acta Mater. **46**, 5929 (1998).
[4] V. I. Levitas, V. F. Nesterenko, and M. A. Meyers, Acta Mater. **46**, 5947 (1998).
[5] T. C. Wu, W. A. Basset, P. C. Burnley, and M. S. Weathers, J. Geophys. Res. **98**, 19767 (1993).
[6] J. J. Gilman, Science **274**, 65 (1996).
[7] V. I. Levitas, in *High Pressure Surface Science and Engineering*, edited by Y. Gogotsi and V. Domnich (Institute of Physics, Bristol, 2004), pp. 159–292.
[8] V. I. Levitas, Phys. Rev. B **70**, 184118 (2004).
[9] J. J. Kim, Y. Choi, S. Suresh, and A. S. Argon, Science **295**, 654 (2002).
[10] A. A. de Ronde and H. Stünitz, Contrib. Mineral. Petrol. **153**, 699 (2007).
[11] C. R. Hickenboth, J. S. Moore, S. R. White, N. R. Sottos, J. Baudry, and S. R. Wilson, Nature (London) **446**, 423 (2007).
[12] P. W. Bridgman, Phys. Rev. **48**, 825 (1935).
[13] N. S. Enikolopyan, Russ. J. Phys. Chem. **63**, 1261 (1989).
[14] A. A. Zharov, Usp. Khim. **53**, 236 (1984).
[15] V. D. Blank, Y. Y. Boguslavski, M. I. Eremetz, E. S. Izkevich, Y. S. Konyaev, A. M. Shirokov, and E. I. Estrin, Sov. Phys. JETP **87**, 922 (1984).
[16] V. D. Blank, S. G. Buga, M. Y. Popov, V. A. Davydov, and V. Agafonov, New J. Chem. **19**, 253 (1995).
[17] V. D. Blank and S. G. Buga, Instrum. Exp. Tech. **36**, 149 (1993).
[18] S. S. Batsanov, N. R. Serebryanaya, V. D. Blank, and V. A. Ivdenko, Kristallografiya **40**, 650 (1995).
[19] N. V. Novikov, S. B. Polotnyak, L. K. Shvedov, and V. I. Levitas, J. Superhard Mater. **3**, 39 (1999).
[20] V. I. Levitas, Y. Ma, J. Hashemi, M. Holtz, and N. Guven, J. Chem. Phys. **125**, 044507 (2006).
[21] V. I. Levitas, Y. Z. Ma, and J. Hashemi, Appl. Phys. Lett. **86**, 071912 (2005).
[22] Y. Ma, E. Selvi, V. I. Levitas, and J. Hashemi, J. Phys.: Condens. Matter **18**, S1075 (2006).
[23] Y. Z. Ma, V. Levitas, and J. Hashemi, J. Phys. Chem. Solids **67**,

2083 (2006).
[24] V. I. Levitas and O. M. Zarechnyy, J. Phys. Chem. B **110**, 16035 (2006).
[25] W. C. Moss and K. A. Goettel, J. Appl. Phys. **61**, 4951 (1987).
[26] W. C. Moss, J. O. Hallquist, R. Reichlin, K. A. Goettel, and S. Martin, Appl. Phys. Lett. **48**, 1258 (1986).
[27] S. T. Weir, J. Akella, C. Ruddle, T. Goodwin, and L. Hsiung, Phys. Rev. B **58**, 11258 (1998).
[28] S. Merkel, R. J. Hemley, and H. K. Mao, Appl. Phys. Lett. **74**, 656 (1999).
[29] V. I. Levitas, S. B. Polotnyak, and A. V. Idesman, Strength Mater. **28**, 221 (1996).
[30] N. V. Novikov, V. I. Levitas, and A. V. Idesman, High Press. Res. **5**, 868 (1990).
[31] V. I. Levitas and O. M. Zarechnyy, Appl. Phys. Lett. **91**, 141919 (2007).
[32] V. I. Levitas, *Large Deformation of Materials with Complex Rheological Properties at Normal and High Pressure* (Nova Science, New York, 1996).
[33] V. I. Levitas and O. M. Zarechnyy, EPL **88**, 16004 (2009).
[34] V. I. Levitas, J. Mech. Phys. Solids **45**, 1203 (1997).
[35] V. I. Levitas, J. Mech. Phys. Solids **45**, 923 (1997).
[36] Y. Boguslavskii, K. Achmetshakirova, and S. Drabkin, Eur. Phys. J.: Appl. Phys. **3**, 243 (1998).
[37] V. I. Levitas and L. K. Shvedov, Phys. Rev. B **65**, 104109 (2002).
[38] S. B. Polotnyak, J. Superhard Mater. **30**, 82 (2008).
[39] S. B. Polotnyak, J. Superhard Mater. **30**, 163 (2008).
[40] V. I. Levitas, Int. J. Solids Struct. **35**, 889 (1998).
[41] A. V. Idesman, V. I. Levitas, and E. Stein, Int. J. Plast. **16**, 893 (2000).
[42] V. I. Levitas, J. Phys. IV **6**, 55 (1996).
[43] V. I. Levitas, A. V. Idesman, and E. Stein, Int. J. Solids Struct. **35**, 855 (1998).
[44] V. I. Levitas and O. M. Zarechnyy, following paper, Phys. Rev. B **82**, 174124 (2010).
[45] See supplementary material at http://link.aps.org/supplemental/10.1103/PhysRevB.82.174123 for distributions of normal and shear stresses in the sample and along its flat contact surface.
[46] M. M. Aleksandrova, V. D. Blank, and S. G. Buga, Solid State Physics **35**, 1308 (1993).
[47] V. D. Blank, Z. H. Malyushitska, and B. A. Kulnitskiy, High Pressure Physics and Engineering **3**, 28 (1993).
[48] V. Domnich, D. Ge, and Y. Gogotsi, in *High Pressure Surface Science and Engineering*, edited by Y. Gogotsi and V. Domnich (Institute of Physics, Bristol, 2004), p. 381.

Supplementary Material

Modeling and simulation of strain-induced phase transformations under compression in diamond anvil cell

Valery I. Levitas[1†] and Oleg M. Zarechnyy[2]
[1] *Iowa State University, Department of Mechanical Engineering, Aerospace Engineering, and Material Science and Engineering, Ames, Iowa 50011, USA*
[2] *Iowa State University, Department of Aerospace Engineering, Ames, Iowa 50011, USA*
[†] e-mail: vlevitas@iastate.edu

Fields of the normal stresses σ_{zz} and σ_{rr} and shear stresses τ_{rz}

a) Phase transformations for equal yield strength of phases.

In Fig. S1, contour lines of equal values of the normal stresses σ_{zz} and σ_{rr}, as well as shear stresses τ_{rz}, are presented. In Fig. S2, distributions of the normal stresses σ_{zz} and σ_{rr} along the flat contact surface between the sample and the anvil are given.

Normal component σ_{zz} of the stress tensor (Figs. S2,a and S1,a) grows almost linearly towards the sample's center. Contour lines are vertical, which means that stress σ_{zz} is independent of z. Normal component σ_{rr} of the stress tensor (Figs. S2,b and S1,b) grows also almost linearly along the radius but reduces from the contact surface to the plane of symmetry. It has (in contrast to σ_{zz}) only a small reduction near the symmetry axis, probably connected to reduction in volume due to phase transformation. Distribution of the normal component $\sigma_{\phi\phi}$ of the stress tensor is very close to distribution of σ_{rr} here and for all cases below, and that is why we do not present a figure and do not discuss it later in the text. The contribution of three normal stresses to the pressure produces a tendency for the pressure drop near the symmetry axis for large applied force.

Shear stress τ_{zr} (Fig. S1,c) is bounded by the maximum value of the yield strength in shear τ_y. Maximum values of the shear stress appear near the corner at the contact surface of the sample. With an increase of the applied axial force region with maximum possible value of the contact shear stress approaches the center of the sample. Without phase transformation, this region grows monotonously with increasing force. With phase transformation, there is some reduction in this region between steps 1 and 3, after which it grows again. In this region, shear stress is practically independent of r and reduces monotonously to zero at the symmetry plane.

b) Phase transformations to a stronger high-pressure phase.

Shear stress τ_{zr} at the contact surface (Fig. S3,c) reaches the yield stress in shear in the major external part of a sample before phase transformation starts. At further loading, shear stress increases at the central part of the disc, and the region with $\tau_{zr} > \tau_{y1}$ extends toward the periphery of a sample, repeating approximately the plot $c(r)$. At step 6, when phase transformation is completed in the major part of a sample, in some ring shear stress reaches the yield strength in shear of the high-pressure phase. For this case, the region in which τ_{zr} grows from the yield strength in shear of the low-pressure phase to that of the high-pressure phase coincides with the diffuse interface between phases. The contour lines of τ_{zr} are almost horizontal near the symmetry plane and curved near the contact surface, where τ_{zr} is nonhomogeneous (Fig. S3,c). In the regions of constant contact shear stress, τ_{zr} is practically independent of r and reduces monotonously to zero at the symmetry plane.

Distributions of the normal components $\sigma_{zz} > p$ and $\sigma_{rr} < p$ of the stress tensor at the contact surface (Figs. S4,a and b) are qualitatively similar to pressure distribution. The difference $\sigma_{zz} - \sigma_{rr}$ is proportional to the local yield strength, which grows with concentration c. Stress σ_{zz} practically does not vary along the thickness of the sample. Normal component σ_{rr} (Fig. S3, b) reduces from the contact surface to the plane of symmetry. No reduction in σ_{rr} and p near the symmetry axis is observed, in contrast to the case with equal yield strength.

c) Phase transformations to a weaker phase.

Shear stress τ_{zr} (Fig. S5,c) is distributed very heterogeneously. During compression, it reduces in transforming regions due to reduction in the yield strength until it reaches the yield strength of the high-pressure phase in the completely transformed region at the contact surface. Local oscillations can be seen both at the contact surface and in the bulk. The normal components of the stress tensor σ_{zz} and σ_{rr} at the contact surface are distributed similarly to the pressure (Figs. S6,a and b). There is a plateau in the same ring. Pressure drop in the region of arrested phase transformation is larger for σ_{rr} than for pressure and smaller or absent for σ_{zz}. The distribution of σ_{zz} is practically independent of z, as it is for both other cases. The normal component σ_{rr} reduces from the contact surface to the symmetry plane.

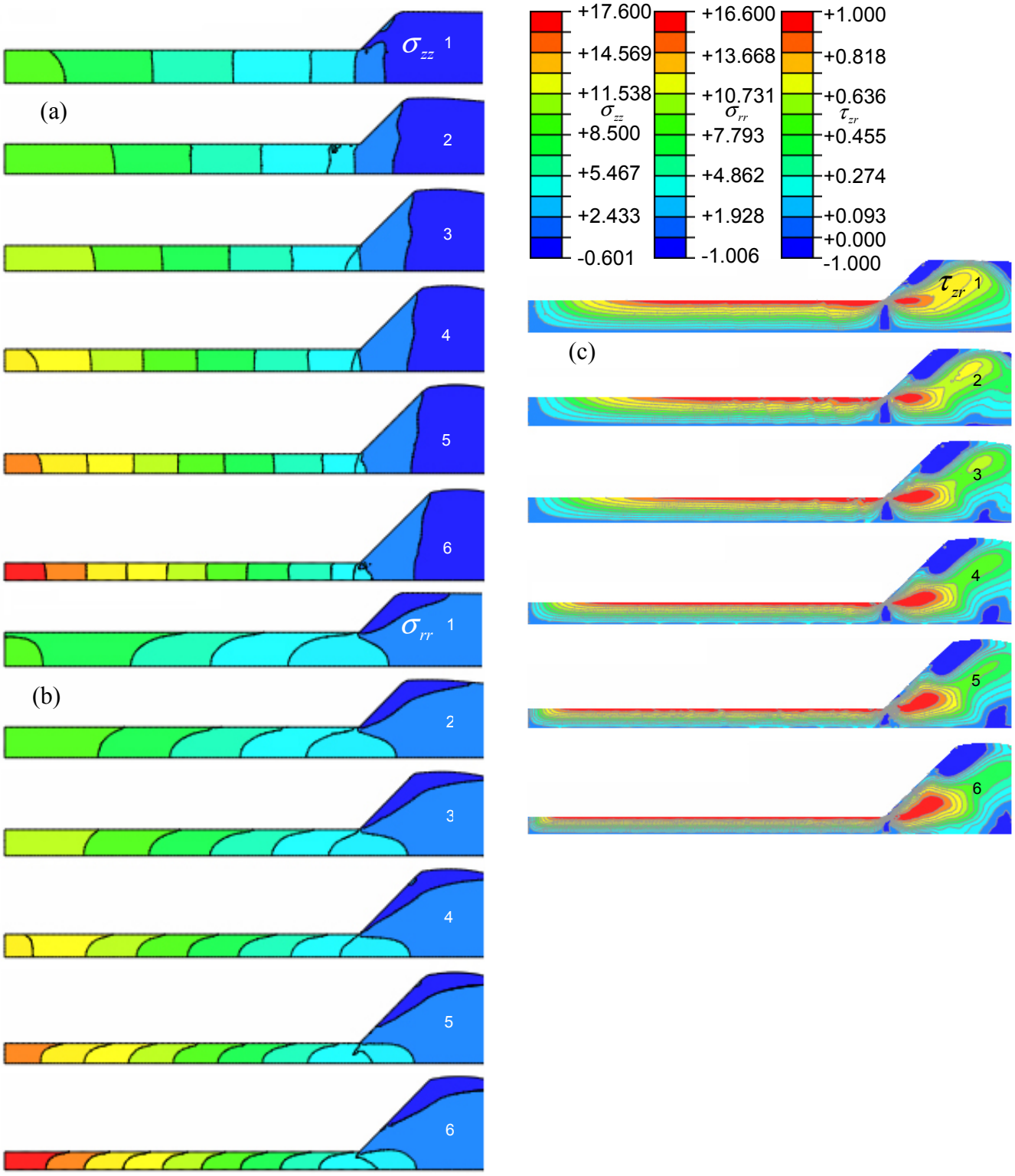

FIG. S1. Distribution of normal stress σ_{zz} (a), normal stress σ_{rr} (b), shear stress τ_{zr} (c) for the case with $\sigma_{y2} = \sigma_{y1}$ for different values of the dimensionless applied axial force F. 1: $F = 4.29$, 2: $F = 4.83$, 3: $F = 5.50$, 4: $F = 6.09$, 5: $F = 6.73$, 6: $F = 7.44$.

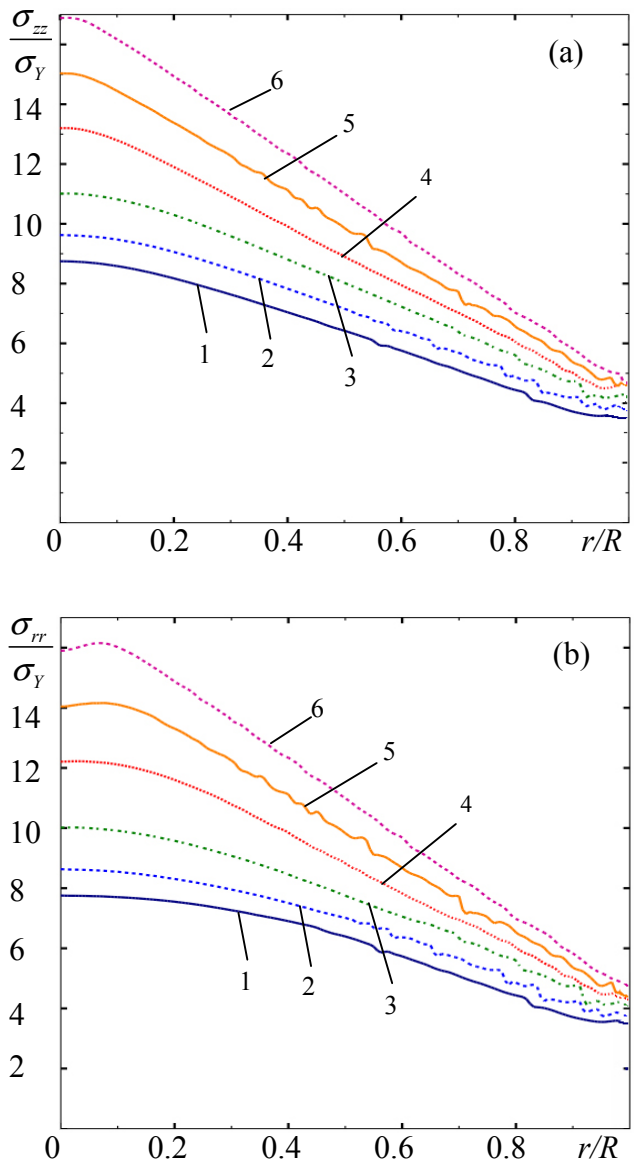

FIG. S2. Distribution of normal axial stress σ_{zz} (a) and normal radial stress σ_{rr} (b) along the radius of the contact surface of a sample r for the case with $\sigma_{2y} = \sigma_{1y}$ for different values of the dimensionless applied axial force F. 1: $F = 4.29$, 2: $F = 4.83$, 3: $F = 5.50$, 4: $F = 6.09$, 5 : $F = 6.73$, 6 : $F = 7.44$.

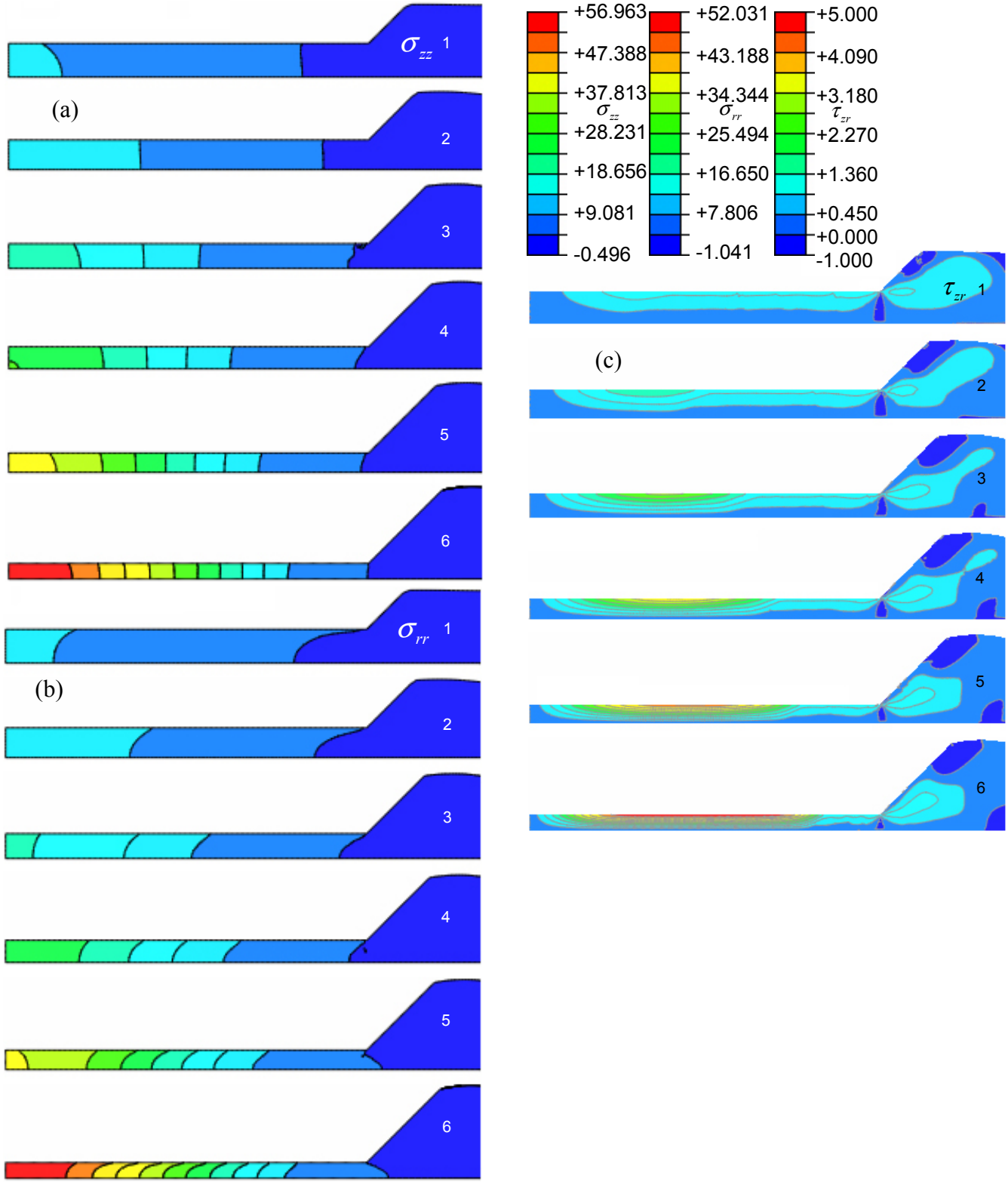

FIG. S3. Distribution of normal stress σ_{zz} (a), normal stress σ_{rr} (b), and shear stress τ_{zr} (c) for the case with $\sigma_{y2} = 5\sigma_{y1}$ for different values of the dimensionless applied axial force F. 1: $F = 4.29$, 2: $F = 5.09$, 3: $F = 6.74$, 4: $F = 8.39$, 5 : $F = 11.05$, 6 : $F = 15.56$.

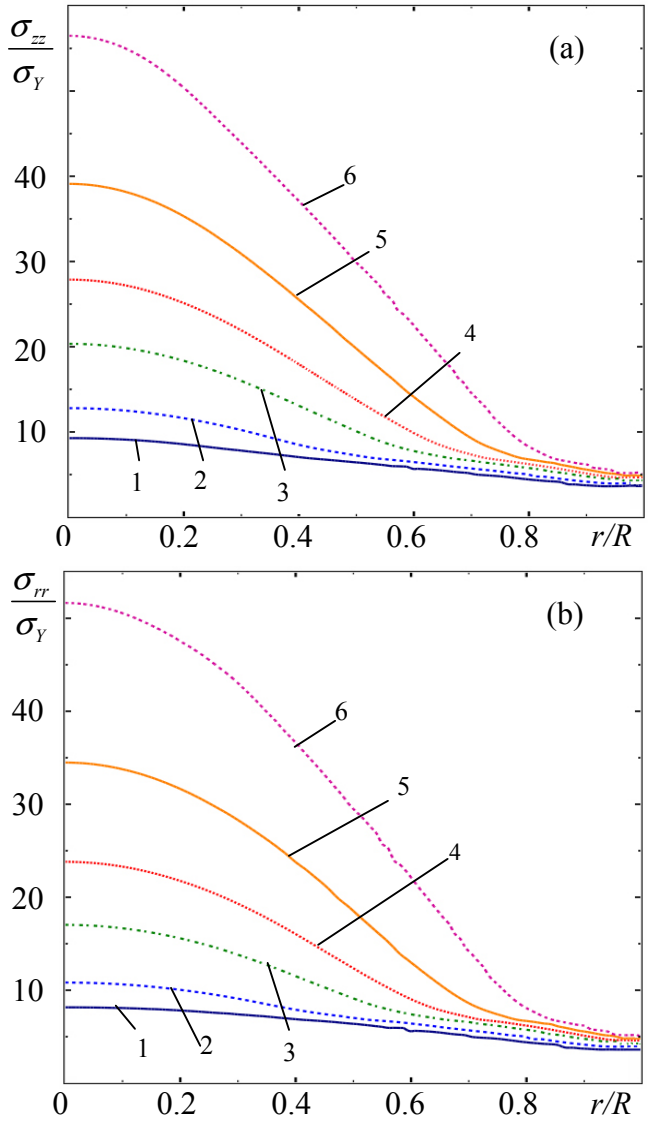

FIG. S4. Distribution of normal stress σ_{zz} (a) and σ_{rr} (b) along the radius of the contact surface of a sample r for the case with $\sigma_{2y} = 5\sigma_{1y}$ for different values of the dimensionless applied axial force F. 1: $F = 4.29$, 2: $F = 5.09$, 3: $F = 6.74$, 4: $F = 8.39$, 5 : $F = 11.05$, 6 : $F = 15.56$.

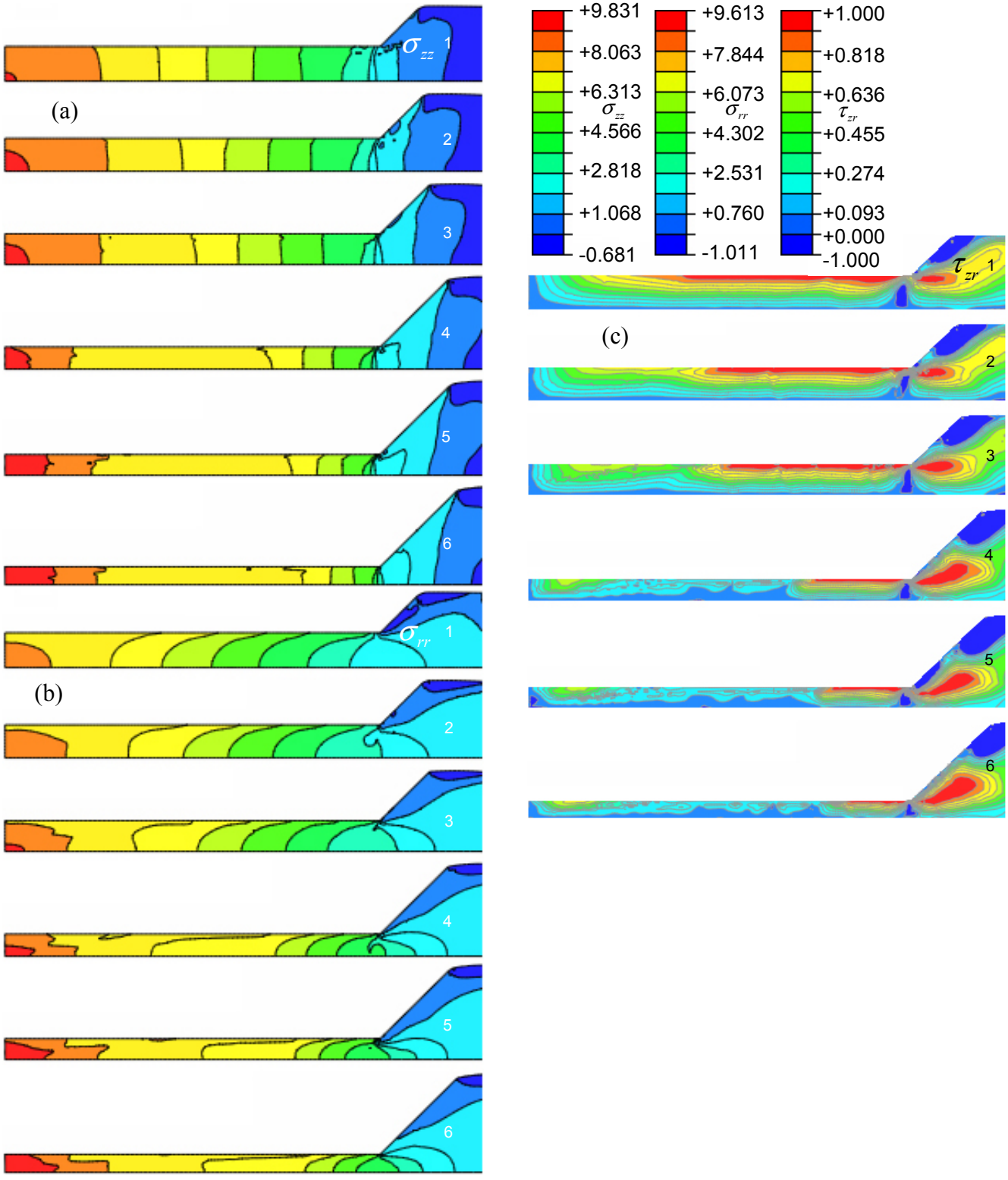

FIG. S5. Distribution of normal stress σ_{zz} (a), normal stress σ_{rr} (b), and shear stress τ_{zr} (c) for the case with $\sigma_{y2} = 0.2\sigma_{y1}$ for different values of the dimensionless applied axial force F. 1: $F = 4.38$, 2: $F = 4.68$, 3: $F = 4.80$, 4: $F = 5.62$, 5 : $F = 5.97$, 6 : $F = 6.10$.

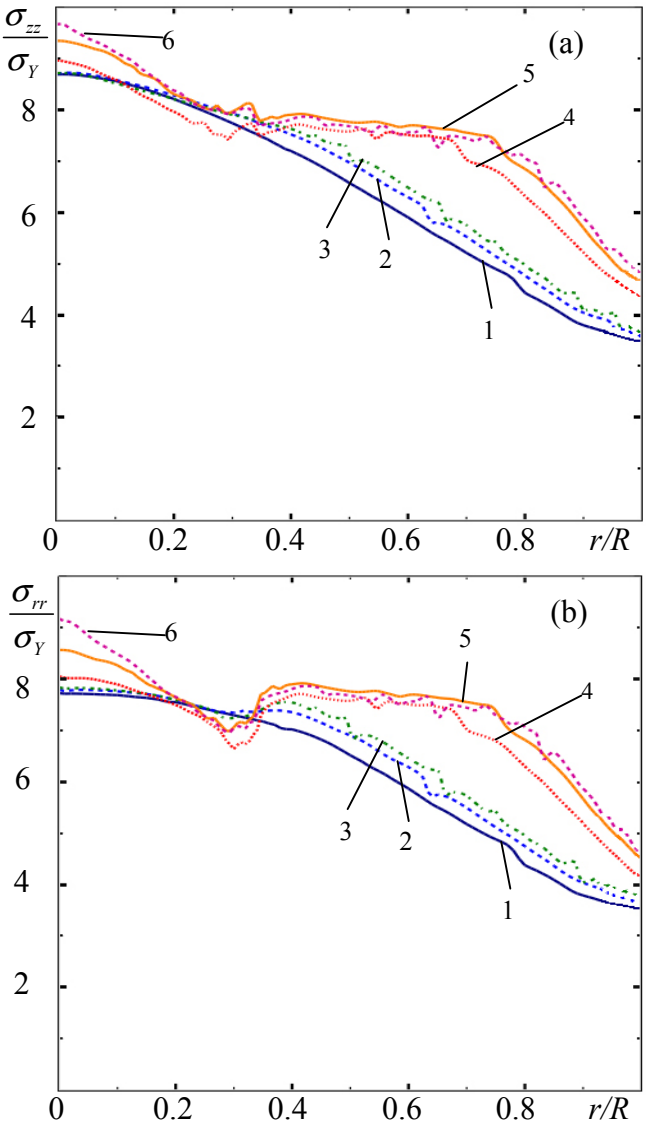

FIG. S6. Distribution of normal stress σ_{zz} (a) and normal stress σ_{rr} (b) along the radius of the contact surface of a sample r for the case with $\sigma_{2y} = 0.2\sigma_{1y}$ for different values of the dimensionless applied axial force F. 1: $F = 4.38$, 2: $F = 4.68$, 3: $F = 4.80$, 4: $F = 5.62$, 5 : $F = 5.97$, 6 : $F = 6.10$.